A Primer to the Interpretation of Refractivity Imagery during IHOP_2002

Frédéric Fabry
McGill University
Montreal, Canada

Crystalyne R. Pettet
National Center for Atmospheric Research
Boulder, Colorado

1. On refractivity and IHOP

The International H_2O Project (IHOP_2002, Weckwerth et al. 2003) sought to determine the extent with which improved characterization of the water vapor field will result in significant, detectable improvements in warm-season quantitative precipitation forecast (QPF) skill. To this end, a large number of instruments were deployed over a seven-week period in late spring 2002 in the Southern Great Plains of the United States (Oklahoma, Kansas, and Texas) to collect data with an unprecedented resolution on humidity, temperature, and winds. Specific goals included improving our understanding of convection initiation and of boundary layer processes, assessing the changes in QPF skill from improved moisture measurements, as well as instrumentation testing and evaluation. One of the instruments present during IHOP_2002 was NCAR's S-Pol radar making measurements of near-surface refractive index fields.

The refractive index n of a medium is defined as the ratio of the speed of light in vacuum and the speed of light in that medium. At low levels, n is typically around 1.003, and its range of values rarely spans more than 100 ppm at any given location. For convenience, a derived quantity called the refractivity N is typically used where $N = 10^6 (n-1)$. In the troposphere, N has been showed to depend on pressure (P), temperature (T), and water vapor pressure (e), following

$$N = 77.6 \frac{P}{T} + 3.73 \times 10^5 \frac{e}{T^2} = N_{dry} + N_{wet}, \quad (1)$$

with the pressures being in hectopascals and temperature in degrees Kelvin (Bean and Dutton 1969). While the first term proportional to air density is larger (225–325 vs. 0–150), most of the spatial variability in N results from the second term barring major changes in temperature associated with fronts or storm outflows: a change in 1 N-unit can be caused by a change of 1°C in temperature or of 0.2 hPa in vapor pressure which corresponds to 0.2°C in dew point temperature at 18°C. Qualitatively, fields of N can hence be seen as proxies for fields of humidity during the summer. Quantitatively, given an average pressure and temperature over the radar coverage, humidity can be recovered with reasonable accuracy (Fabry and Creese 1999).

As refractivity changes, so does the speed of light as well as the number of radar wavelengths between the radar and fixed ground targets (Fig. 1). This slight change in the number of wavelengths between the radar and targets manifests itself by a change in the phase ϕ of these targets, which can be measured by the radar and then used to calculate refractivity. If enough fixed ground targets are present, which is often the case within a 40 km radius of the radar, fields of refractivity can be obtained by radar with a spatial resolution of the order of a few kilometers.

Many atmospheric phenomena, whether associated with boundary layer processes, mesoscale or synoptic events, are caused by or result in gradients or variability in surface moisture. Through the refractivity measurement, these gradients can be sampled and observed by radar. Radar measurements of refractivity now give us a rare glimpse at the mesoscale variability of moisture in the same manner measurements of radar reflectivity gave us our first view of the mesoscale structure of precipitation half a century ago. The measured N fields proved to be surprisingly rich in information despite the ambiguity associated with the conversion of N into humidity and especially the limited spatial coverage of the coverage. In parallel, very few researchers have been exposed to refractivity imagery and know what kind of information one can obtain from it, or have any knowledge of the potential problems and data quality issues surrounding the derivation of the refractivity field. Here we will try to introduce the potential data user to some of these issues.

$$\phi_i = 2\pi f\, t_{travel} = \frac{4\pi f\, r_i}{c}\, \overline{n(0 \to r_i)}$$

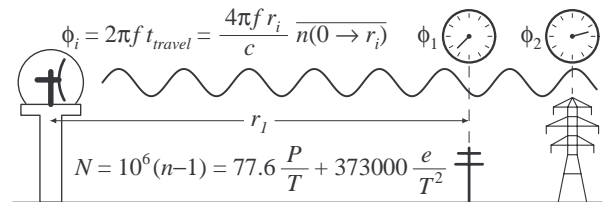$$N = 10^6 (n-1) = 77.6 \frac{P}{T} + 373000 \frac{e}{T^2}$$

FIG. 1. Illustration of the concept behind the measurement of the refractivity N by radar. The phase ϕ_i of targets at range r_i from the radar is determined by the frequency f of the radar and the time of travel t_{travel} between the radar and the target. As the refractive index of air n between the radar and the target changes, the speed of radar waves c/n is altered, as a result of which both t_{travel} and the measured ϕ_i are also modified. By measuring the phase of fixed ground targets, one can obtain n and compute the refractivity of air, a parameter related to pressure, temperature, and vapor pressure.

At calibration time

A) Get time series of phase maps in constant n regime (n = n_{ref})

ϕ_{ref}

Average them together; this is the map of reference phase ϕ_{ref}

B1) Use the average SNR to identify echoes from sidelobes

SNR

Echoes from sidelobes

B2) Measure a time series of scan-to-scan phase differences

$\dfrac{d\phi}{dt}$

B3) Compute temporal coherence of dφ/dt from the ratio of lag-1 and lag-0 time correlation

And use the sidelobe detection to mask out sidelobe contamination

Notes:

Calibration steps A and B do not need to be done for the same time sequence. Step A requires very uniform n for a few scans. Step B needs a few hours of data without weather echoes, preferably with some wind and without major changes in n near the surface.

Changes in n over a short time period Δt can be computed by replacing ϕ_{ref} by $\phi(t - \Delta t)$ at step IV.

RI

The result is the ground target reliability index map

In real-time

I) Measure the phase of targets and other parameters (SNR, v, σ)

ϕ

Precip. clutter

SNR

II) Use SNR, v, σ to select ground targets

QI

This is the target quality index

III) Take minimum of QI and RI to make the weighting function

IV) Subtract reference phase

$\phi\text{-}\phi_{ref}$

WF

V) Smooth phase difference over small areas using the weighting function

$\phi\text{-}\phi_{ref}$
(smoothed)

VI) Derive path values of n from slopes of phase difference

n

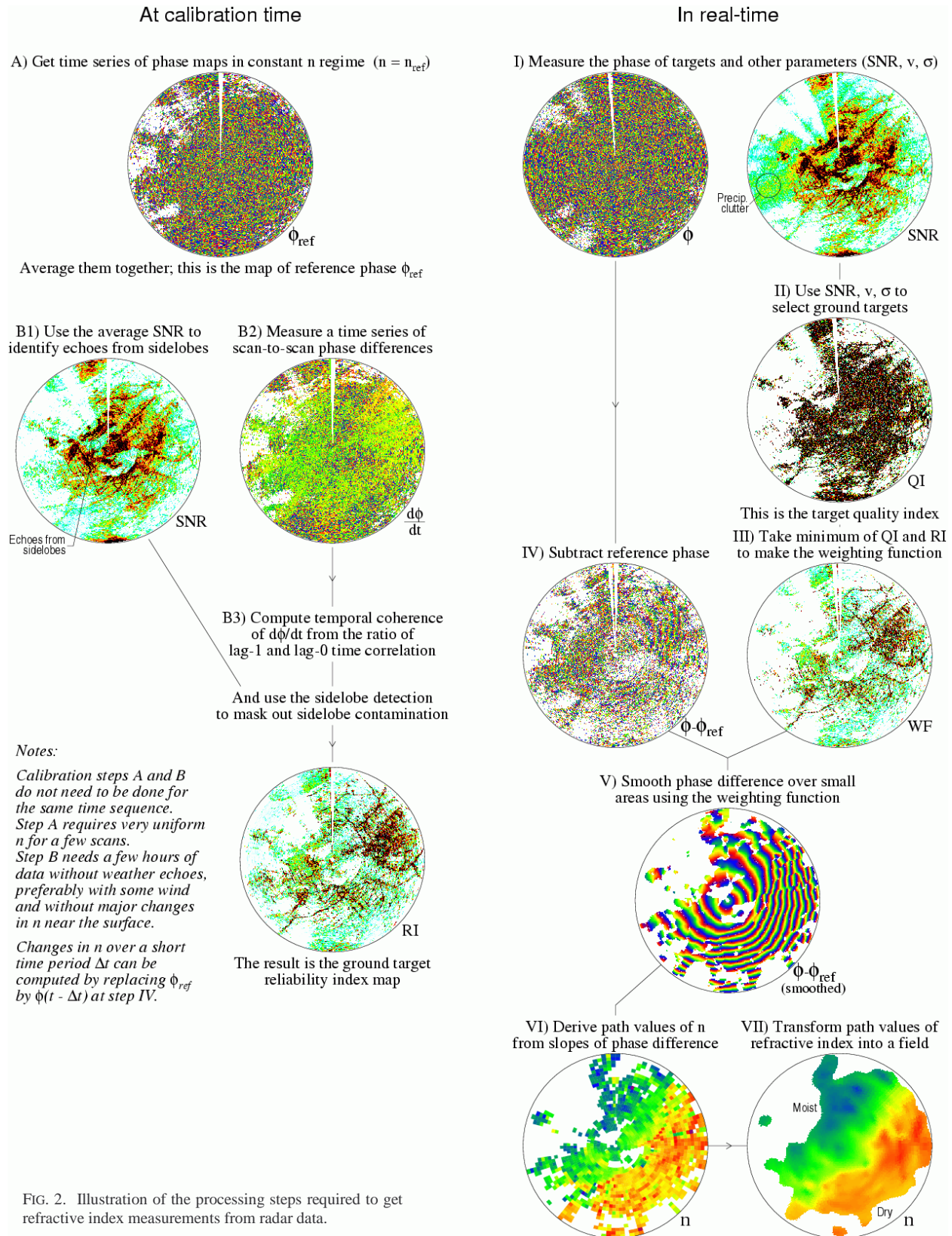**VII) Transform path values of refractive index into a field**

Moist

Dry

n

FIG. 2. Illustration of the processing steps required to get refractive index measurements from radar data.

2. Extraction of refractivity maps

a) Background

Refractivity is obtained by monitoring the change in the phase ϕ of a target between the present time t_1 and a reference time t_0, as ϕ is used as a proxy for the travel time t_{travel} between the radar and that target:

$$\Delta\phi = \phi(t_1) - \phi(t_0) = \frac{4\pi f}{c} \int_0^r \left(n(x,y,z,t_1) - n(x,y,z,t_0) \right) dr'$$

(2)

Equation (2) illustrates the fact that the quantity that can truly be measured by radar is the *change* between a reference time and the current time of the *path-integrated* refractive index between the radar and a target, provided that target is absolutely stationary. There are hence some assumptions and processing steps required to obtain 2-D maps of refractivity or refractive index.

The main assumption is that all targets are perfectly aligned. If one has two targets T_1 and T_2 along the same azimuth, one may try to use (2) twice, first between the radar R and T_1, and then between R and T_2, in order to get n between T_1 and T_2 by making the difference, e.g.

$$\begin{aligned} \Delta\phi(T_2) - \Delta\phi(T_1) &= \left(\phi(T_2,t_1) - \phi(T_2,t_0) \right) - \left(\phi(T_1,t_1) - \phi(T_1,t_0) \right) \\ &= \frac{4\pi f}{c} \left(\int_0^{r(T_2)} n(r',t_1) - n(r',t_0) dr' \right. \\ &\quad \left. - \int_0^{r(T_1)} n(r',t_1) - n(r',t_0) dr' \right) \\ &\approx \frac{4\pi f}{c} \left(\int_{r(T_1)}^{r(T_2)} n(r',t_1) - n(r',t_0) dr' \right). \end{aligned}$$

(3)

The advantage of this approach is that if T_1 and T_2 are close enough to each other, it becomes impossible to have changes of n large enough for $\Delta\phi(T_2) - \Delta\phi(T_1)$ to alias, something that is extremely likely to happen (see step V on Fig. 2). The caveat is that for (3) to work, the paths R-T_1 and R-T_2 must be exactly collinear, which means that the radar, T_1, and T_2 must be aligned. This alignment must be fairly accurate on the horizontal and especially on the vertical plane for (3) to be exact. Since this is rarely the case with "natural" ground targets, the phase difference data for such pair of targets will be extremely noisy except perhaps when t_1 and t_0 to each other. Contending with this noise is the major challenge facing the refractivity algorithm.

The second main assumption behind the derivation of refractivity is that there is a reference time t_0 for which we know $n(x,y,z,t_0)$ for all (x,y) near the surface. This is generally not the case. The reference values $n(x,y,z,t_0)$ are determined by choosing a time period where n is as constant as possible based on available surface data, computing $n(t_0)$ or n_{ref} from the surface stations, and declaring that the phase data measured during that period are representative of what one would expect if the refractive index n is equal to n_{ref} everywhere.

The general process of deriving refractivity fields is illustrated in Fig. 2. First, at calibration, two sets of data are collected, one for determining where the fixed targets to be used by the algorithm are located (step B of Fig. 2), and one for the calibration of the phase data for these targets (step A of Fig. 2) when $n = n_{ref}$. Then, at the time of interest, after having identified the "good" ground targets (step II and III of Fig. 2), one computes $\Delta\phi$ (step IV) using (2). As advertised, the data are extremely noisy; a smoothing step is therefore required (step V) as n is obtained from the derivative in range of $\Delta\phi$ (step VI). Finally, the refractivity data may then be additionally smoothed (step VII).

Note that in addition to n, it is possible to compute a change in n over a short time period without the need of the calibration step by using the phase data measured at the beginning of the time period of interest as a reference. Although $\Delta n/\Delta t$ maps are harder to interpret, they are usually more precise and often reveal weak signals that would remain undetected in the noisier n data.

b) IHOP_2002 implementation

During the field campaign, a short time period early in the project on May 14 between 20:10 and 20:40 was used for calibration. After post-field reanalysis, it turned out that this time period was the period of most uniform refractivity observed by surface stations for the whole project. Hence, in terms of calibration, the field-computed refractivity maps available on the JOSS field catalog (www.joss.ucar.edu/ihop/catalog/), and the final product maps (to be) available on the JOSS IHOP data sets site (www.joss.ucar.edu/ihop/dm/archive/), are nearly identical (refractivity calibration was done over a somewhat larger time period in the post-field analysis). That being said, significant differences exist between the two sets as a result of a modification in the processing program to convert phase data into n maps and the disabling of the final smoothing step (step VII on Fig. 2) to obtain maps of greater spatial resolution. On the minus side, the new reanalysis program is, at the current stage, considerably more hesitant at using data in regions of precipitation where the phase data might be corrupted by rain or hail clutter ☺ (the field version of the program did not identify weather echoes because the ground-echo-filtered S-Pol Doppler data could not be used to evaluate the quality of ground returns).
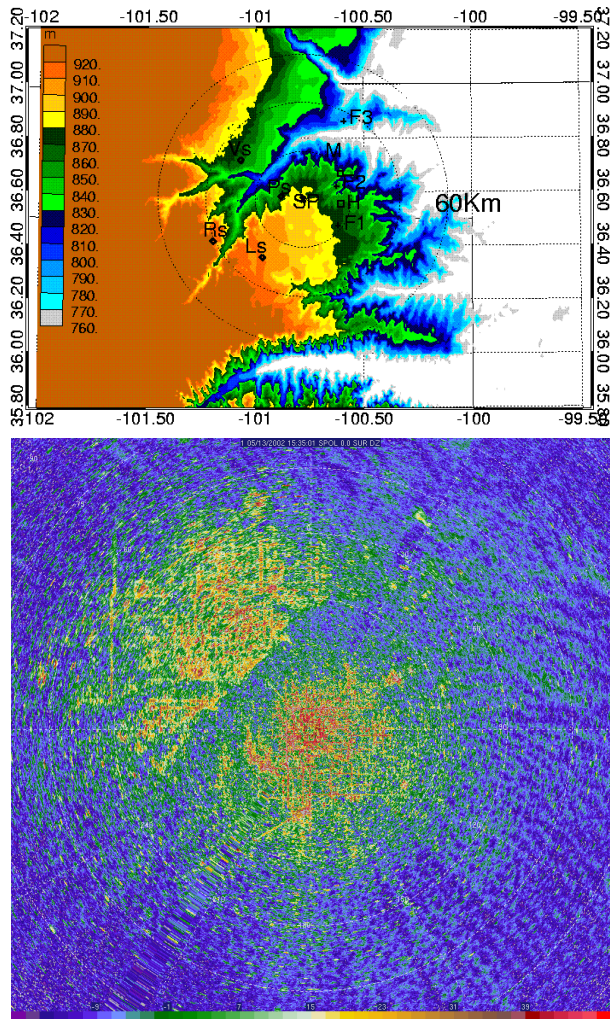
FIG. 3. Elevation map (top), 0° PPI of reflectivity of the ground echoes observed (middle), and illustration of the area of data coverage (below) of refractivity measurements during IHOP_2002. Elevation map courtesy of ShinJu Park (McGill University).

FIG. 4. The S-Pol radar in the field (sic!) during IHOP_2002. Photo courtesy of Jeff Keeler (NCAR/ATD).

3. Data coverage

S-Pol was deployed in the middle of an agricultural field in the Oklahoma Panhandle near Bryan's Corner (Fig. 4). Despite what is hinted by the photograph, it turned out that 1) there was a noticeable amount of change in ground elevation in the area and 2) there were enough E-W and N-S aligned power and telephone poles, in addition to farm buildings and towers to provide the large number of fixed echoes required to compute fields of refractivity (Fig. 3). As a result of the local topography, the area of data coverage forms a relatively small disk of 50 km diameter centered slightly SE of S-Pol and a significant arc in the NW quadrant extending from 25 to 60 km range of S-Pol, with the Beaver River Valley separating the two regions.

4. Parameters computed

Four data fields were computed for the whole project whenever S-Pol data was available:

• An S-Pol level refractivity field. If the refractivity at calibration had been perfectly uniform, one could use (2) and (3) to generate a refractivity map near ground level. In IHOP_2002, uniform refractivity was never achieved at calibration because of the spatial distribution in surface pressure caused by the change in terrain elevation over the coverage area. The N measurements computed are hence biased by a location dependent constant that depends on the difference in elevation (and pressure) between the reference level taken to be the height of the surface station nearest to the S-Pol radar (883 m) and the elevation of the targets from which the radar measures the phase. Typical corrections will be of the order of a few N units. If one chose not to do this correction, one can still use the data by assuming that it is the refractivity one would have

measured if all the targets were at 883 m (somewhat like a "potential refractivity measurement at S-Pol level"). For example, comparisons with surface stations would hence be done by first correcting the station pressure to S-Pol level, and then computing refractivity from the station data using (1).

• *Scan-to-scan change in the refractivity field*. This field was also computed using (2) and (3), except that instead of using the reference time as t_0, one uses the time of the previous scan. Because the $\Delta\phi$ data from scan to scan is considerably cleaner than the $\Delta\phi$ over a period of several weeks used in refractivity maps, the resulting fields are more precise and more detailed. But

the interpretation of these maps can be misleading, since the signatures in N and in ΔN are typically radically different even though they are mathematically related (Fig. 5). For example, when advection occurs, ΔN maps tend to erase stationary or along-flow gradients such as those associated with rolls and fine lines while enhancing cross flow gradients such as outflows and fronts. Care must hence be taken to ensure that one does interpret properly what one sees as well as what does not see on such maps.

• *Error fields of N and ΔN*. These two fields are estimates of the error on the measurement of N and ΔN. They are experimental fields designed to help the use of refractivity information for data assimilation. They capture reasonably well the normal error of refractivity retrievals associated with the noisy input phase fields, but fail to catch the occasional blunder of the algorithm (more details in Section 5). Errors associated with the noisy phase data typically have long time correlations (of the order of six hours, but strictly speaking inversely proportional to the rate of change of dn/dz) and have a $(1 - \Delta x^2/4)(1 - \Delta y^2/4)$ correlation in space where Δx and Δy are the E-W and N-S displacements in km. Blunders on the other end have typically (though not always) little time continuity.

All fields are defined everywhere within 67.5 km of the radar, even though true data coverage is smaller. Accurate or at least useful refractivity measurements can be identified by the magnitude of the error field. In general, if the error on N or ΔN exceeds 20 N units, the data has no value. This threshold is what was used in the summary displays such as the one in Fig. 6 that are (or will be) available on the JOSS web site.

Examples of N difference fields

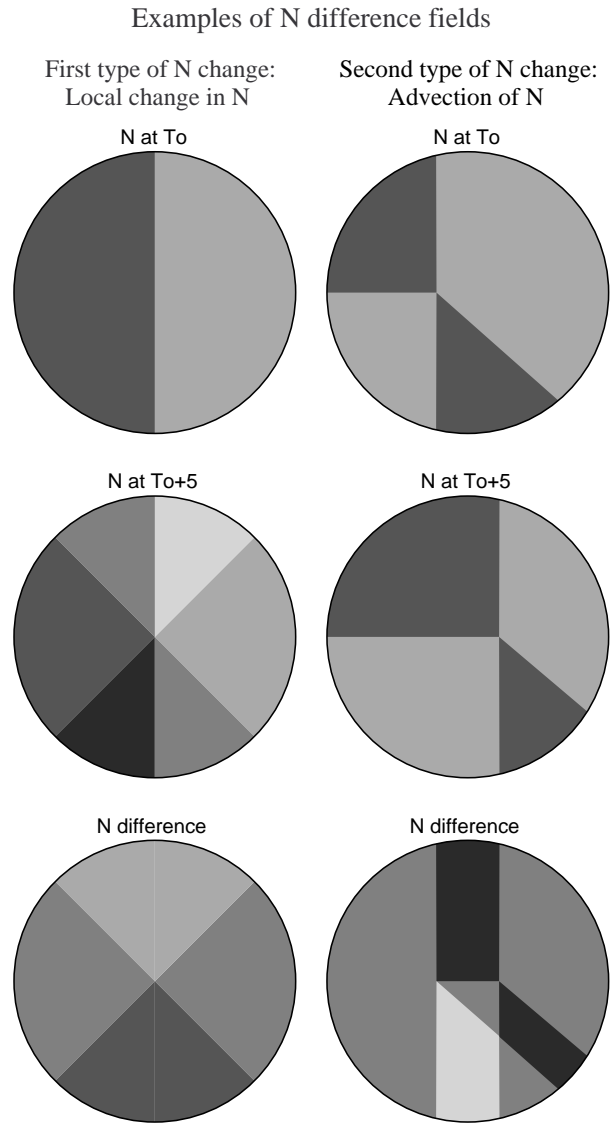| First type of N change: Local change in N	Second type of N change: Advection of N

FIG. 5. Illustration using synthetic examples of the type of fields one might expect on the scan-to-scan N difference map. Changes may be local (due to warming or vertical fluxes of N, left column) or caused by advection (of a front – top half of each screen – or of a local extremum in N – bottom half of each screen –, right column).
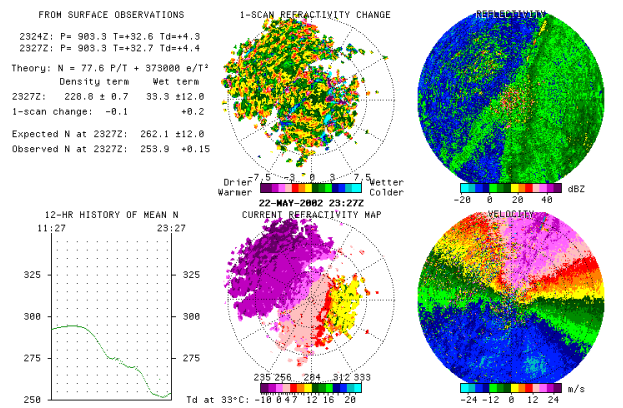

FIG. 6. Summary display (similar to the images produced in the field) of the derived refractivity information. It includes a summary of surface observations from the 9 stations within S-Pol coverage (upper left), a 12-hr history of mean refractivity (lower left), and fields of scan-to-scan refractivity change (upper center) and of refractivity (lower center). 0° PPIs of reflectivity (upper right) and Doppler velocity (lower right) provide additional contextual information.

5. Data quality issues

a) Additional information on N calibration

The quality of the refractivity field obtained depends on the degree of with which the $\Delta\phi$ data used to compute N is "smooth" (a very relative term most of the time) or noisy. Noisiness in $\Delta\phi$ is primarily a function of the lack of alignment of targets in the vertical (a property of the "site") combined with how different the current vertical structure of n (or dn/dz near the ground) is from the one at the calibration time (a function of weather conditions; Fig. 7). The 14 May calibration was done during daytime in relatively dry conditions, when dn/dz was close to zero or in slight subrefraction conditions. When dn/dz is vastly different, e.g. at night or in other conditions closer to superrefraction, the algorithm might have difficulties recovering N near the surface especially at further range. This results in both a small reduction in data coverage as well as in an increase in regions where N is inaccurately retrieved.

To mitigate that problem, we chose to use, in combination with the original 14 May calibration, a second calibration period on 21 May during the night around 9:00Z for cases when dn/dz was closer to the type of conditions one would expect at night. To minimize biases and artificial jumps associated with a change in the reference used, the calibration data obtained with 21 May was "homogenized" to the 14 May calibration by modifying it at a scale of a few kilometers so the output of the algorithm gave similar results. Despite these efforts, it is likely that there will be small "jumps" in refractivity values at times when the calibration file was changed, especially for point values (as opposed to for large areas). Table 1 lists the time periods (UTC) used for each reference. The choice of the time periods was made by visually inspecting the output fields computed using both calibrations, and choosing the one that had the fewest data errors and the largest coverage, while trying to avoid having a reference transition in the middle of a particularly interesting event.
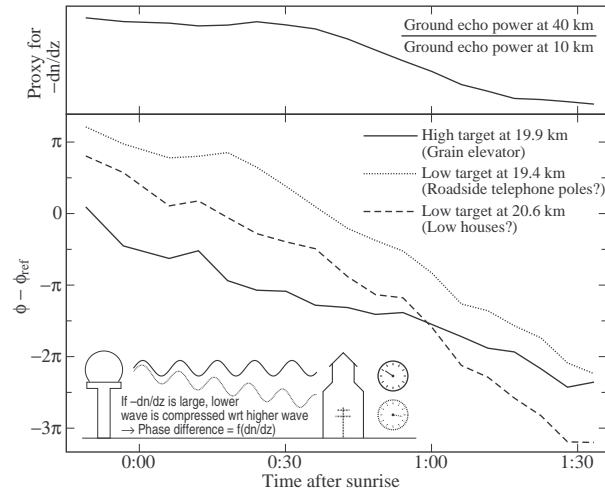

FIG. 7. Time evolution of the phase of three neighboring targets aligned on the same azimuth during the disappearance of trapping conditions immediately after sunrise. The phases of the two low level targets (dotted and dashed lines) parallel each other because similar changes in path-integrated n occur in the two low-level paths between the radar and these targets. In between these low-level targets is a higher target whose phase (solid line) does not vary as much because the change in path-integrated n along the higher-level path is smaller. This occurs as a result of an adjustment in dn/dz as we move from trapping conditions (illustrated in the inset above by the stronger reflections of faraway targets) to normal propagation conditions. During trapping conditions, the higher target only 20 km away (in Perryton TX) was about 180° out of phase compared to what it would have been under normal propagation conditions. This phenomenon introduces noise in the $\Delta\phi$ field.

TABLE. 1. Calibration used for different time periods.

14 May calibration	21 May homogenized calib.
11 May 1500 → 14 May 0300	14 May 0300 → 14 May 1400
14 May 1400 → 16 May 1000	16 May 1000 → 19 May 1600
19 May 1600 → 19 May 2300	19 May 2300 → 21 May 1500
21 May 1500 → 23 May 0600	23 May 0600 → 25 May 2000
25 May 2000 → 26 May 0000	26 May 0000 → 26 May 1800
26 May 1800 → 26 May 2200	26 May 2200 → 29 May 1800
29 May 1800 → 30 May 0100	30 May 0100 → 30 May 1800
30 May 1800 → 31 May 0100	31 May 0100 → 31 May 1700
31 May 1700 → 01 June 0100	01 June 0100 → 01 June 1700
01 June 1700 → 02 June 0100	02 June 0100 → 02 June 1700
02 June 1700 → 03 June 0900	03 June 0900 → 03 June 2000
03 June 2000 → 04 June 0100	04 June 0100 → 07 June 2000
07 June 2000 → 08 June 0100	08 June 0100 → 08 June 1500
08 June 1500 → 09 June 0000	09 June 0000 → 09 June 1400
09 June 1400 → 10 June 0000	10 June 0000 → 10 June 1400
10 June 1400 → 10 June 1800	10 June 1800 → 11 June 2000
11 June 2000 → 12 June 0200	12 June 0200 → 12 June 1000
12 June 1000 → 12 June 1400	12 June 1400 → 14 June 1800
14 June 1800 → 14 June 2200	14 June 2200 → 15 June 2000
15 June 2000 → 15 June 2330	15 June 2330 → 18 June 0000
18 June 0000 → 18 June 0200	18 June 0200 → 18 June 1500
18 June 1500 → 19 June 0800	19 June 0800 → 19 June 1300
19 June 1300 → 20 June 0200	20 June 0200 → 20 June 2200
20 June 2200 → 21 June 0300	21 June 0300 → 21 June 1400
21 June 1400 → 22 June 0400	22 June 0400 → 22 June 1400
22 June 1400 → 23 June 0400	23 June 0400 → 23 June 1300
23 June 1300 → 24 June 0800	24 June 0800 → 24 June 1500
24 June 1500 → 25 June 0300	25 June 0300 → 25 June 1500
25 June 1500 → 26 June 0000	

b) Recognizing mistakes of the algorithm

Despite the fact we generally chose the *N* map with the least amount of mistakes, they will nevertheless occur occasionally. Here we will try to briefly illustrate how to recognize them.
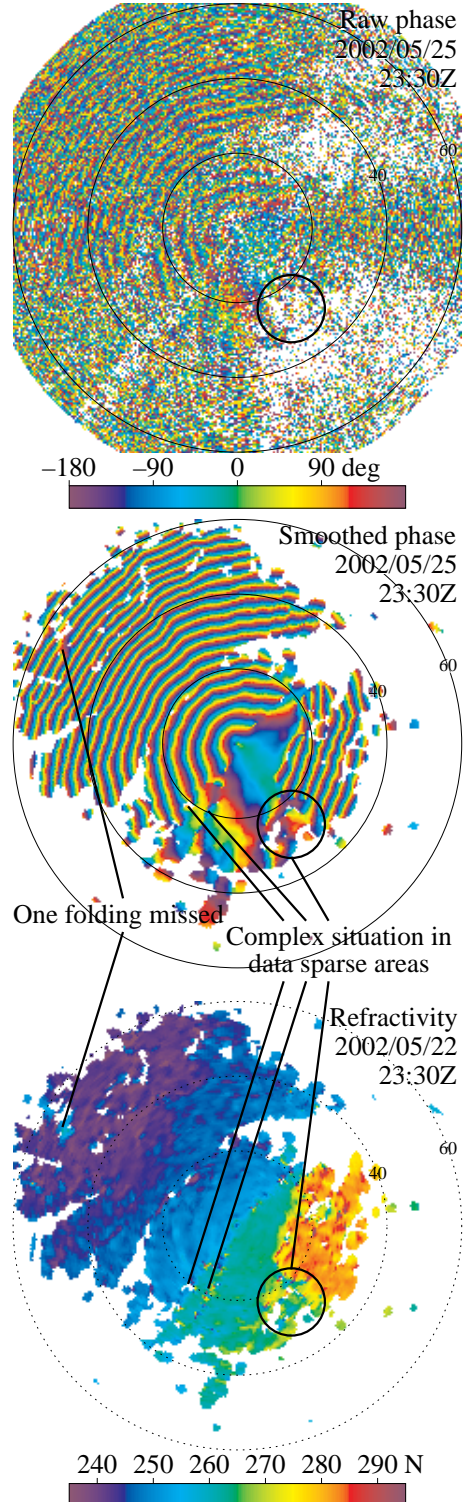

Raw phase
2002/05/25
23:30Z

−180   −90   0   90 deg

Smoothed phase
2002/05/25
23:30Z

One folding missed

Complex situation in
data sparse areas

Refractivity
2002/05/22
23:30Z

240 250 260 270 280 290 N

FIG. 8. Illustration of the transformation of phase data into *N* data. Top: Raw $\Delta\phi$ as obtained after subtracting the reference. Note the noisiness of the data whose magnitude at this time was slightly smaller than average for IHOP_2002 S-Pol data. Middle: $\Delta\phi$ after a 4 by 4 km smoothing. Regions where the smoothing gave poor results have been detected by the algorithm and rejected. Despite this, there are areas where the smoothing washed out unobvious but crucial details, resulting in an error locally. Bottom: *N* field resulting from the smoothed phase field. Errors crept in regions where a 360° cycle was missed as well as in areas of *N* gradients and downrange of them where the phase data proved too confusing to be properly smoothed.

Refractivity is computed from $d\Delta\phi/dr$, with $\Delta\phi$ being a noisy field. Since the derivative of a noisy function is an even noisier function, one must try to smooth the $\Delta\phi$ to obtain reasonable results. In our case, we smooth $\Delta\phi$ over a 4 km by 4 km area independent of range. This generally allows us to get phase data smooth enough to be differentiated at the cost of losing most of the sub 4-km variability in *N*. But smoothing phases that may span more than 360°, something very likely to happen in a 4 km by 4 km area, is particularly challenging, especially if refractivity gradients occur over regions where "ground echo quality" is low. As a result, mistakes occasionally occur (Fig. 8). These mistakes will cause a local blunder in *N*, and sometimes fool the program in believing that $d\Delta\phi/dr$ has changed for good, biasing all the values at ranges beyond that point.

There are a few sets of "failure modes" that can be recognized by visually inspecting the data.

• *The biased radial.* Often originating from a region where significant gradients in *N* occur, on azimuth 150 in Fig. 9, or from data sparse regions, in this case on both sides of azimuth 330. Because data quality becomes lower in these radials, they will often look as if they are full of holes.
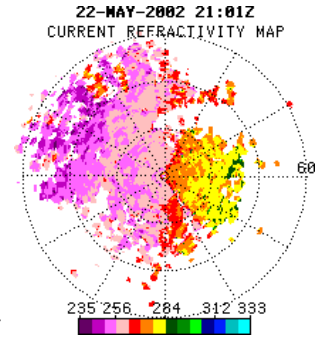

FIG. 9. Biased radials example.

• *The biased small pocket.* It can have a variety of origins. It may be by itself, generally resulting from a missed 360° cycle (NW on Fig. 8), or in couplets either along an azimuth or at the same range on either side of a sharp *N* gradient.

• *Suspicious changes near the edge of data coverage.* Anything unusual happening either on the edge of the Beaver River Valley or at the edge of the data coverage should generally be looked at with suspicion.

• *Halo around S-Pol.* For unknown reasons, data immediately around S-Pol (< 3 km) seem unreliable and occasionally form a "halo" of 2 km radius. It is most likely the effect of a bug still to be tracked down in the *N* retrieval algorithm.

In general, the best way to determine if something unusual is real or an error is to look at an animation of a time sequence of images. If the oddity cannot be tracked in time and appears and disappears instead, it is probably an error (Fig. 10). That being said, biased radials can sometimes be somewhat persistent in time
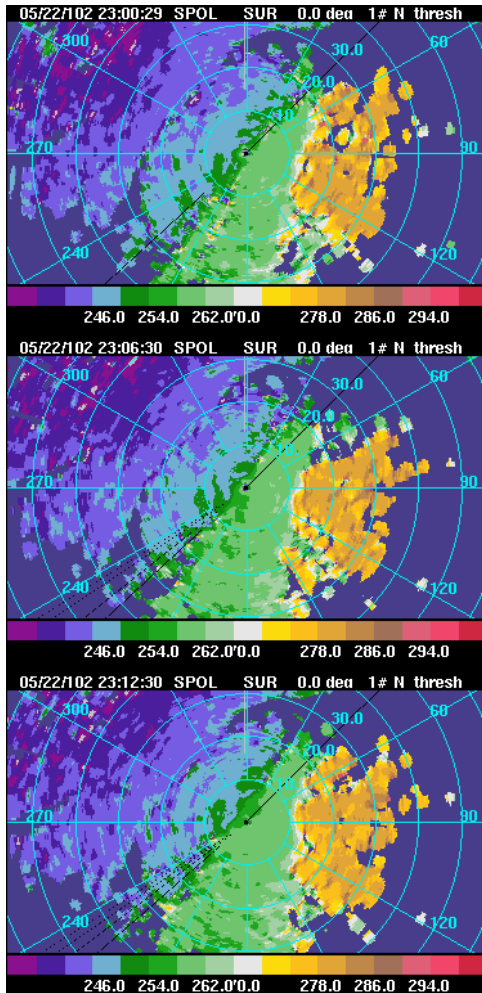
FIG. 10. Time sequence of refractivity showing the type of errors in *N* estimates one can expect to find. These include primarily local errors such as the yellow and purple "dots" to the SW, as well as one or two examples of faulty radials (e.g. SE on the middle image). The lack of time continuity of these signatures contrasting with the consistency of other features helps us recognize what is real from what is not. Note that the black solid and dotted lines SW and NE of the radar are artifacts of the display software used to generate this figure.

too. Another trick is to look at other fields such as reflectivity to see if some large changes in *N* might be expected as a result of precipitation or a convergence line.

6. Summary of observations

Refractivity data was collected whenever 0° PPI or surveillance scans were made by S-Pol. Those were typically done every 5 minutes for the whole project except during short periods of radar breakdown and during some of the stormy events early in the project. Figure 11 gives an impressionist view of the type of data that was collected during IHOP_2002. The top of

Figure 11 shows the histogram of refractivity observed as a function of time. It illustrates the diurnal cycle of N data and the range of values being observed at any time, with dark narrow areas corresponding to very uniform conditions and wide or multimodal light areas being indicative of noticeable gradients in moisture within the small data coverage area. Since it covers the whole field experiment, it gives an unbiased view of the refractivity variability over a long period and allows the reader to get a better appreciation of the frequency of occurrence of the examples to follow.
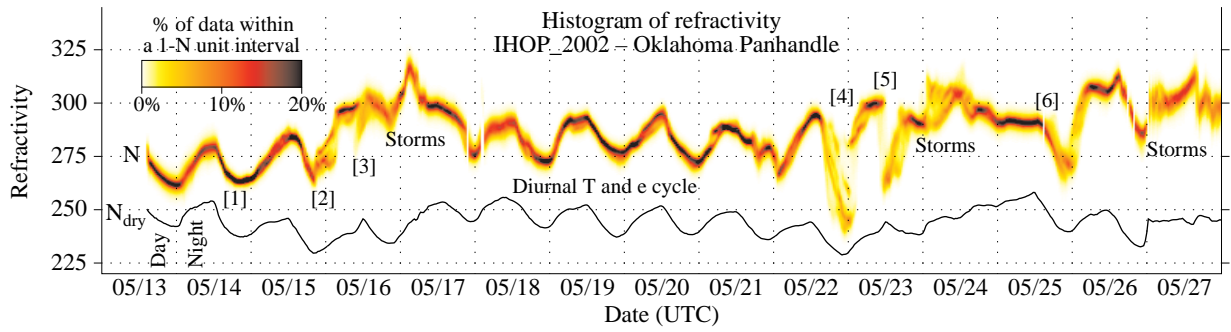
Twelve sets of examples of refractivity imagery are then provided in the bottom part of Figure 11 associated with different signatures in the histogram. Examples cover a wide variety of phenomena: larger scale moisture boundaries such as those associated with fronts (note [5] in Fig. 11), drylines and other convergence lines ([4], [12] and [13]), gust fronts and outflows ([8], [10], [11]), or less sharp gradients of unclear origin ([7] and [10]); boundary layer (BL) phenomena such as rolls ([14]), more cellular structures ([1]), and uneven moistening of the BL by surface fluxes ([6]); and finally, nocturnal waves ([9] and [10]). As this list suggests, refractivity data could hence be of considerable interest not only to meteorologists concerned with convection initiation, but also to researchers in boundary layer processes.

Two special data sets were also collected. On 16 May between 19:50 and 20:25, the radar essentially made a long set of consecutive 0° surveillance scans every 45 s or so to look at small scale changes in refractivity associated with a windy and partly cloudy day. Then, on 9 June, with an approaching gust front ([10], left), the radar was fixed in azimuth, first pointing in the direction roughly perpendicular to the approaching gust front (00:16:25 – 00:21:42, azimuth 125°), and then pointing approximately along the axis of the gust front (00:21:53 – 00:27:33, azimuth 10.5°) as it passed over S-Pol.
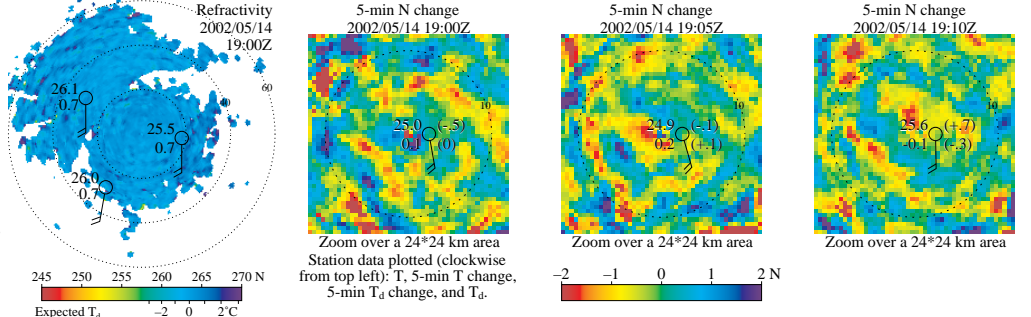
REFERENCES

Bean, B.R., and E.J. Dutton, 1968: *Radio Meteorology*. National Bureau of Standards Monogr., No. 92, National Bureau of Standards, 435 pp.

Fabry, F., and C. Creese, 1999: If fine lines fail, try ground targets. Preprints, 29th Int. Conf. on Radar Meteorology, Montreal, Canada, Amer. Meteor. Soc., 21-23.

Fabry, F., 2004: Meteorological value of ground target measurements by radar. *J. Atmos. Oceanic Technol.*, in press.

Weckwerth, T. M. D. B. Parsons, S. E. Koch, J. A. Moore, M. A. LeMone, B. B. Demoz, C. Flamant, B. Geerts, J. Wang and W. F. Feltz, 2003: An overview of the International H2O Project (IHOP_2002) and some preliminary highlights. *Bull. Amer. Meteor. Soc.*, in press.

Histogram of refractivity
IHOP_2002 – Oklahoma Panhandle

% of data within a 1-N unit interval

0%   10%   20%

[1] Day-time data in a uniform air mass. Although no large-scale N gradients are visible (first image), small-scale boundary layer structures may be tracked on the time series of 5-minute refractivity differences (far right), although considerable change occurs.

Refractivity
2002/05/14
19:00Z

5-min N change
2002/05/14 19:00Z

5-min N change
2002/05/14 19:05Z

5-min N change
2002/05/14 19:10Z

Zoom over a 24*24 km area
Station data plotted (clockwise from top left): T, 5-min T change, 5-min T_d change, and T_d.

Zoom over a 24*24 km area

Zoom over a 24*24 km area

245 250 255 260 265 270 N
Expected T_d −2   0   2°C

−2   −1   0   1   2 N

[2] Gradual sharpening of a moisture gradient associated with a reflectivity fineline. Similar to but not as impressive as [4].

[3] Cold front passing over the area with a dew point decrease behind it.

[4] One of the banner days for refractivity, as a main dryline and a few secondary drylines gradually built up over the area. Interestingly, the build-up of the boundaries was detected with refractivity before one could clearly observe any reflectivity finelines. This might be related to the fact that it takes time for the updrafts associated with the convergence lines to lift enough insects to permit their detection using reflectivity.

Refractivity
2002/05/22
22:48Z

240 250 260 270 280 290 N
T_d −5   0   5   10°C
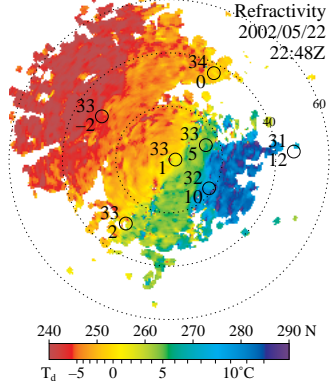
[5] Image of the change in refractivity over a 5-min period during the passage of a cold front over a 60 by 60 km area. This image reveals that, behind the initial change in temperature and moisture along the front boundary is a 15-km wide transition zone over which the refractivity (associated with the dew point and real temperatures) continues to decrease until it reaches its final value.

5-min N change ending 2002/05/23 11:34Z

−4   −2   0   2 N
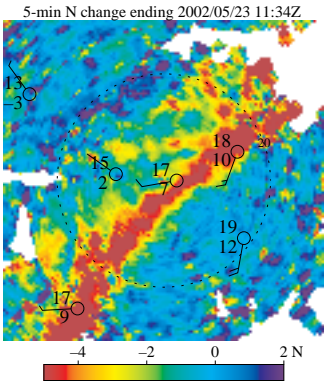
[6] Thanks to very weak winds and uneven rain in the previous days (first image), we observed the gradual appearance of regions with different humidity (far right) solely caused by the variable surface moisture fluxes as a function of soil moisture.

1   2   5   10 15 20 30 50 mm
24-hr accumulation ending 05/24 12Z

Refractivity
2002/05/25
13:03Z

285 290 295 300 305 310 N
T_d 0   2   4   6°C

Refractivity
2002/05/25
17:02Z

275 280 285 290 295 300 N
T_d 0   2   4   6   8°C

Refractivity
2002/05/25
19:00Z

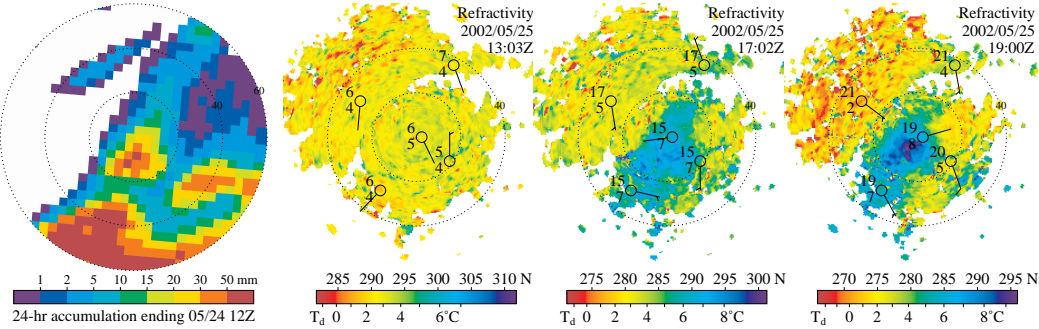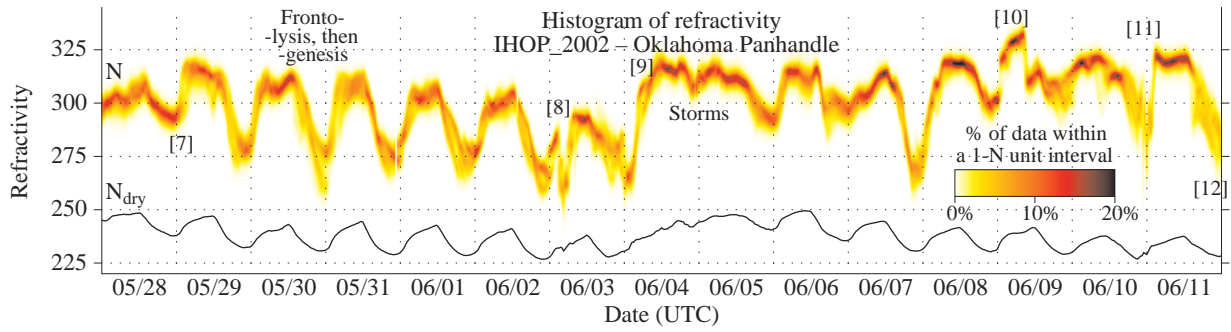270 275 280 285 290 295 N
T_d 0   2   4   6   8°C

FIG. 11. Top: Histogram of refractivity as a function of time observed by the S-Pol radar in the Oklahoma Panhandle from the 13 May to 25 June 2002. The difference between the N_{dry} curve and the color shaded values is proportional to the amount of moisture measured near the ground. Bottom: Mini case studies of individual events annotated on the histogram plot. These include a short text description and a variety of radar data (surface refractivity, 5-min surface refractivity change, and PPIs of reflectivity and of Doppler velocity) and surface observations (often plotted on the refractivity maps, sometimes plotted aside in the form of a time series).

9 of 11

Histogram of refractivity
IHOP_2002 – Oklahoma Panhandle

[7] [8] [9] [10] [11] [12]

N

Storms

N_dry

% of data within a 1-N unit interval

0% 10% 20%

Fronto--lysis, then -genesis

Refractivity (y-axis): 225, 250, 275, 300, 325

Date (UTC): 05/28 05/29 05/30 05/31 06/01 06/02 06/03 06/04 06/05 06/06 06/07 06/08 06/09 06/10 06/11
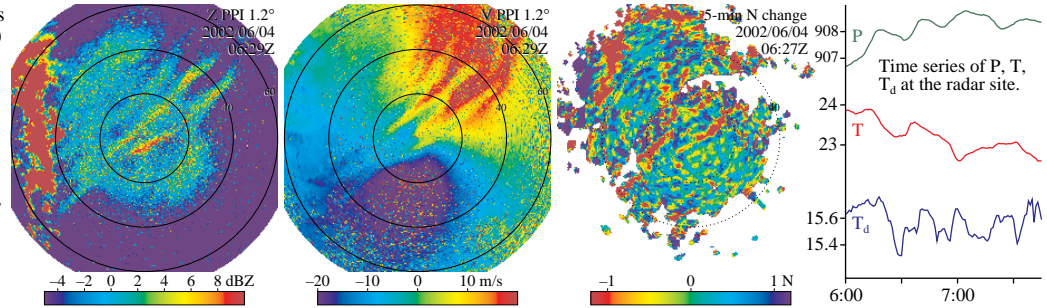
[7] Sudden pulse of surface moisture occurring at the beginning of the night. In this area, nighttime moistening is often associated with the passage of an air-mass boundary coming from the SE early in the night. By contrast, the daytime drying occurs mainly by vertical mixing.
Also note the large difference between N-derived dew point temperatures – representative of data at about 20 m – and the actual surface measurements.
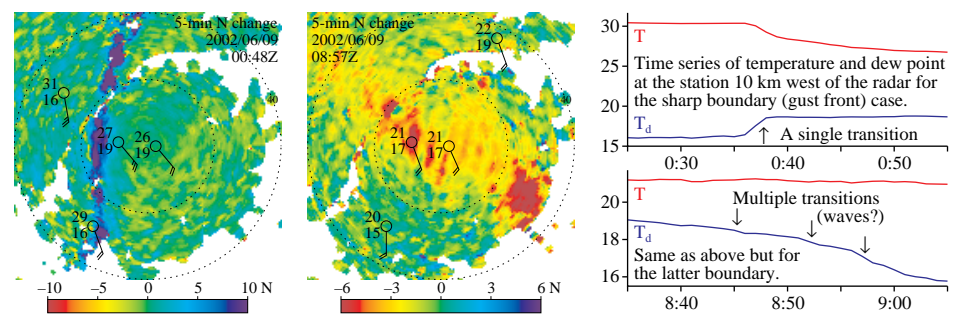
Refractivity 2002/05/29 02:01Z

290 295 300 305 310 315 320 N
T_d 10 12 14°C
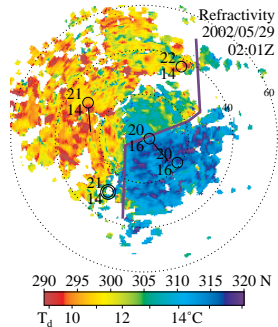
[8] (Multiple?) storm outflow(s) from a line of thunderstorms SW of the radar site. While the reflectivity map shows only one fineline associated with the outflow (solid and dotted line), the refractivity map (right) suggests the presence of multiple boundaries with only an extremely faint refractivity contrast colocated with the reflectivity fineline. In this case, the outflow is relatively warm and dry; in others (e.g. [11]), it is cool and humid.

Refractivity 2002/06/03 02:57Z

Storm cell

Reflectivity fine line

260 270 280 290 N
T_d 0 5 10°C
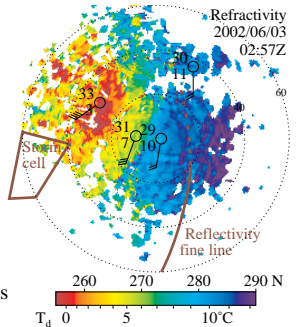
[9] Nighttime bore as seen on (left to right) reflectivity, Doppler velocity and 5-min refractivity change. At this time, the bore is barely detectable on refractivity as pressure waves show some correlation with dew points. Case analyzed by Koch et al. (2003).

Z PPI 1.2° 2002/06/04 06:29Z

−4 −2 0 2 4 6 8 dBZ

V PPI 1.2° 2002/06/04 06:29Z

−20 −10 0 10 m/s

5-min N change 2002/06/04 06:27Z

−1 0 1 N

Time series of P, T, T_d at the radar site.

P: 908, 907
T: 24, 23
T_d: 15.6, 15.4

6:00 7:00

[10] Two examples of refractivity boundaries: a sharp temperature and moisture boundary (caused here by a gust front), and a diffuse moisture transition a few hours later. Both the refractivity change maps and the surface data (far right) show the different nature of the boundaries. The latter example displays hints of a wave structure within it, not an uncommon occurrence for nighttime boundaries.

5-min N change 2002/06/09 00:48Z

−10 −5 0 5 10 N

5-min N change 2002/06/09 08:57Z

−6 −3 0 3 6 N

Time series of temperature and dew point at the station 10 km west of the radar for the sharp boundary (gust front) case.
T, T_d: 30, 25, 20, 15
↑ A single transition

0:30 0:40 0:50

Multiple transitions (waves?)
T, T_d: 20, 18, 16
Same as above but for the latter boundary.

8:40 8:50 9:00

[11] Very high range of refractivity values caused by the presence of multiple storm outflows.
Such conditions cause problems to the algorithm retrieving refractivity fields; hence, data quality is poorer than usual and the field shows considerable fragmentation.
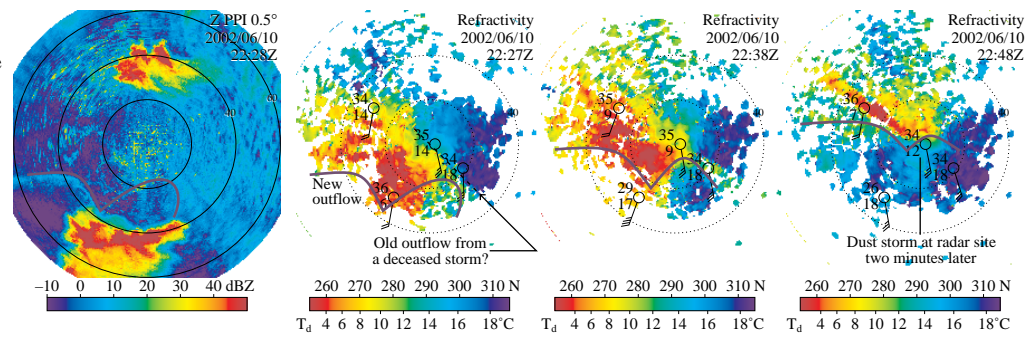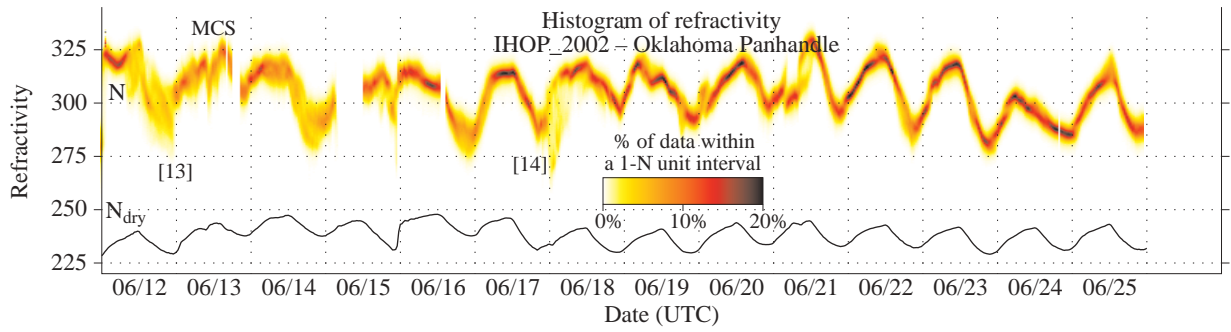
Z PPI 0.5° 2002/06/10 22:28Z

−10 0 10 20 30 40 dBZ

Refractivity 2002/06/10 22:27Z

New outflow

Old outflow from a deceased storm?

260 270 280 290 300 310 N
T_d 4 6 8 10 12 14 16 18°C

Refractivity 2002/06/10 22:38Z

260 270 280 290 300 310 N
T_d 4 6 8 10 12 14 16 18°C

Refractivity 2002/06/10 22:48Z

Dust storm at radar site two minutes later

260 270 280 290 300 310 N
T_d 4 6 8 10 12 14 16 18°C

FIG. 11. (continued)

Histogram of refractivity
IHOP_2002 – Oklahoma Panhandle

[12] Here, the relatively wide range of refractivity values observed is associated with the presence of a convergence line just NW of the radar site (visible on reflectivity as a fineline (right) as well as on refractivity (far right)). Although clouds poked through the capping inversion (see photo below from S-Pol), no storm initiated.
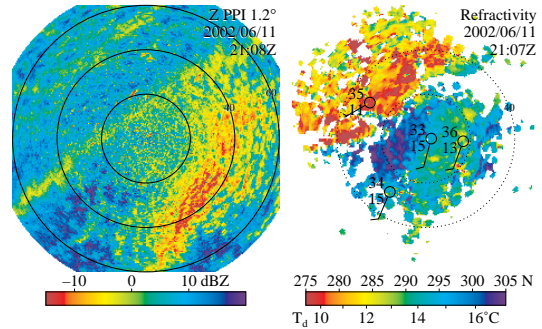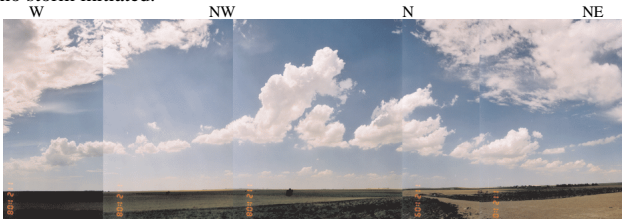
[13] On this day, a weak low pressure system was forming over S-Pol. A persistent slow-moving dry pocket drifted to the southern edge of the refractivity coverage. By 2336Z, a boundary had built up and was moving south (see the refractivity and refractivity change maps on the right). In parallel, a gust front coming from the south can be seen on the reflectivity map (far right) 60 km from the radar. These two boundaries collided 45 min later and a severe thunderstorm initiated 30 km east of S-Pol as a result.
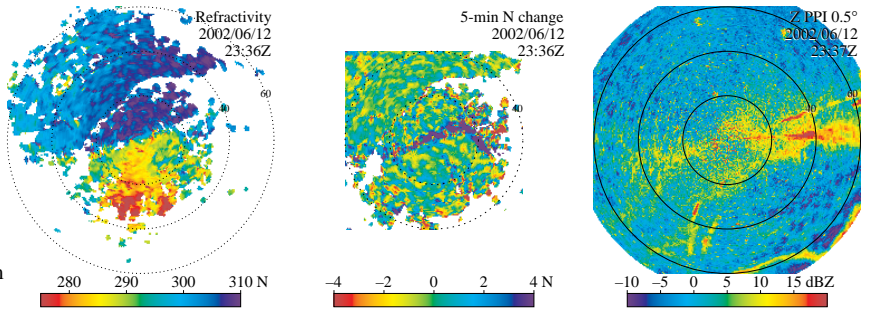
[14] Example of smaller scale variability in refractivity caused by the boundary layer structure on a sunny and windy day. At this time (about 14:00 solar time), BL rolls can be observed on reflectivity (first image). On refractivity (second image), when two images are averaged (19:59 and 20:04) to remove the cross-roll variability, one may observe some along-roll refractivity structure superposed on a stronger larger scale moisture variability. The 5-min refractivity change map (far right), that enhances cross-wind N variability, reveals the presence of cross-roll N structure as well.
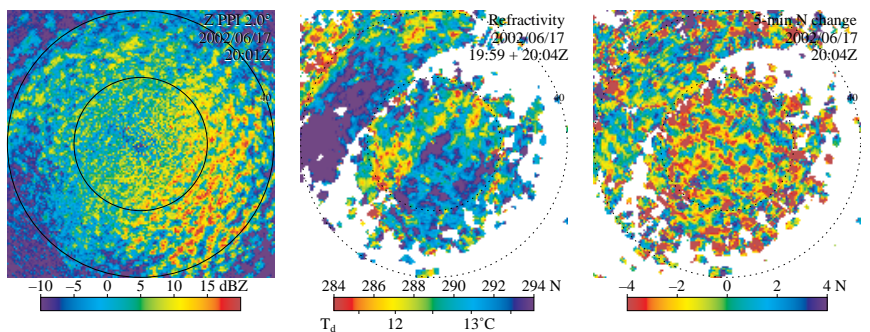
FIG. 11. (end)